Construction of S-N-C bond for boosting bacteria-killing by synergistic effect of photocatalysis and nanozyme

Longwei Wang [a,b,1], Zhongwei Yang [a,1], Guoxin Song [a], Zhen You [b,c], Xiaoyu Zhang [b,c], Lin Liu [a], Jian Zhang [d], Longhua Ding [a], Na Ren [a], Aizhu Wang [a,*], Jing Liu [b,c,**], Hong Liu [a,e], Xin Yu [a,*]

[a] Institute for Advanced Interdisciplinary Research, School of Chemistry and Chemical Engineering, University of Jinan, Jinan 250022, PR China
[b] CAS Key Laboratory for Biomedical Effects of Nanomaterials and Nanosafety and CAS Center for Excellence in Nanoscience, National Center for Nanoscience and Technology of China, Beijing 100190, PR China
[c] Key Laboratory of Resource Biology and Biotechnology in Western China Ministry of Education School of Medicine, Northwest University, Xi'an 710069, PR China
[d] Department of Biology and Biological Engineering, Chalmers University of Technology, Kemivägen 10, 41296 Göteborg, Sweden
[e] State Key Laboratory of Crystal Material, Shandong University, Jinan 250100, PR China

ABSTRACT

Bacterial infection-related diseases are major public safety issues leads to millions of deaths annually. Herein, a porous sulfur doped graphitic carbon nitride (g-SCN) for ecofriendly, metal-free and low systemic toxicity were synthesized. Sulfur doping enables to broaden the absorption spectrum and promote the photocarriers separation for photocatalysis enhancement. Moreover, sulfur element will coordinate with nitrogen, changing the electronic state and endowing g-SCN with the property of nanozyme. More importantly, we established different models and confirmed that S-N-C coordination is the source of peroxidase (POD)-like activity through theory and experiment. The increased specific surface area of g-SCN, ascribing to the porous structure, makes it easier to trap bacteria. With the synergistic effect of photocatalysis and nanozyme, the prepared g-SCN has the ability to kill both gram-negative and gram-positive bacterium, with an antibacterial efficiency up to 100%. This work provides innovative synergistic strategy for constructing nanomaterials for highly efficient antibacterial therapy.

1. Introduction

In recent years, bacteria are constantly evolving and resistant to our frontline drugs to form super-bacteria due to abuse of antibiotics and fungicides [1–4]. From 2000–2018, the resistance of bacteria to antibiotics in the world has almost tripled, which had important consequences for ecological environment and human health [5]. It reveals the need for more effective sterilization technologies. With the advancement of optical technologies and development of photocatalysis, antibacterial photocatalytic therapy (APCT) has become one of the most promising therapeutically strategies for microbial infections [6–9]. Under the irradiation of light, the photoexcited electrons or holes can react with surrounding oxygen (O_2) or water (H_2O) during the photocatalytic process to generated reactive oxygen species (ROS), which would have peroxidation reaction with cell wall (or cell membrane), leading to the leakage of cytoplasmic components, and finally lead to the death of microorganisms [10–13].

At present, the commonly used photocatalytic antibacterial agents mainly include semiconductor materials, such as metal oxides, metal sulfides and graphitic carbon nitride-based nanomaterials [14–17]. Kangmin Lee et al. developed a TiO_2 coated crystalline silicon microwires array system, which could absorb more the 95% of sunlight over a wide range (300–1000 nm) [18]. As a ROS generator with a long diffusion about 9 μm, its bactericidal effect within 15 min is equivalent to 3 mM H_2O_2. Cui's group developed a Cu deposition vertically aligned few-layered MoS_2 film, which displayed an antibacterial efficiency more than 99.999% within 20 min [19]. In our previous work, we also prepared a heterostructure of C_3N_4/PDINH [20]. Due to its band-matching

relationship, electrons transited from the HOMO level of C_3N_4 to the LUMO level of PDINH with the band gap 1.64 eV, which extended the range of light utilization to 750 nm (NIR-I region).

Although photocatalytic antibacterial has good efficacy, *in vivo* antibacterial treatment, the poor penetration ability of the visible light and the hypoxic microenvironment of the infection site usually reduce its bactericidal effect [21]. This is also one of the reasons why photocatalytic sterilization has not been popularized on a large scale. Referring to the current issues, we propose a mechanism for synergistic bactericidal therapy by using photocatalysis and nanozyme. Nanozymes are nanomaterials with similar active centers or electron transfer structures to naturel enzymes [22–26]. They have the ability to regulate ROS levels, which could destroy the biofilms and biological macromolecules of bacteria [27,28]. Meanwhile, nanozymes have biocompatibility, high stability and reusability compared with traditional biocidal agents [29]. Therefor nanozymes provided an opportunity for the antibacterial alternative in the application of wound healing. Compared with APCT, nanozyme antibacterial therapy (NABT) does not require light, and the microenvironment of the infection site can be rationally utilized according to the catalytic activity of different nanozymes [30]. Gao et al. report an $AgPd_{0.38}$ nanozymes, which could generate surface-bound ROS selectively kill bacteria over mammalian cells [31]. When used as coating additives, $AgPd_{0.38}$ enabled an inert substrate to inhibit biofilm formation and suppress infection-related immune responses in mouse models. In our previous work, we have developed a dispersed and uniform defect-rich MoS_2/rGO vertical heterostructure material, featuring rough surface and abundant Mo and S vacancies. It exhibited excellent three enzyme-like catalytic activity (including OXD-, POD-, and CAT-like activity), and was used to treat drug-resistant *Escherichia coli* (*E. coli*) and *Staphylococcus aureus* (*S. aureus*) both *in vivo* and *in vitro* [32].

Excellent catalytic activity is one of the prerequisites for the efficient sterilization of nanozyme [33]. In order to improve the catalytic activity of nanozymes, an efficient way is to carry out non-metallic element doping [34]. And the most common is N element doping [35]. Gao's group prepared a N-doped porous carbon nanospheres with four enzyme-like activities [36]. Through the synergistic action of these four enzyme-like activities, it can produce ROS and realize the elimination of tumor. In our previous work, we also proved that after N doping, the originally inactive TiO_2 became TiN nanozyme with high POD-like activity [37]. This is mainly because the electronegativity of N is weaker than that of O, which provides a favorable environment for POD reaction. However, it is very strange that the content of N in graphitic carbon nitride (g-CN) is as high as 64%, it does not show any nanozyme activity. Therefore, it can be inferred that the coordination relationship between N and other elements is the key point affecting nanozyme activity. In addition to N doping, the introduction of S atoms have been used to enhance the intrinsic activity of nanozyme. In addition to N doping, the introduction of S atoms have also been used to enhance the intrinsic activity of nanozyme. Zhu's group synthesized an S/N codoped carbon nanozyme with enhanced POD-like activity [38]. Sui et al. prepared an S doped graphdiyne nanosheet which reveals impressive POD-like activities as well as piezoelectric properties [39].

G-CN is a two-dimensional (2D) layered non-metallic photocatalytic material with unique electronic structure, good stability, suitable band gap and easy synthesis and chemical modification [40–42]. At the same time, the 2D nanosheet structure is beneficial to reduce the diffusion distance of carriers, which can provide high specific surface area so as to expose more catalytic active sites for photocatalysis [43]. At present, g-CN photocatalytic sterilization has caused extensive research [44,45]. Wu et al. used MoO_2/g-CN heterostructure for rapid sterilization under visible light [46]. Wang et al. synthesized g-CN nanosheets as a metal-free photocatalyst for bacterial inactivation [47]. Zhao et al. prepared single-layered g-CN for application of photocatalytic disinfection under visible light irradiation [48]. Raizada's group outline the recent research progress in based Z-scheme and S-scheme photocatalytic
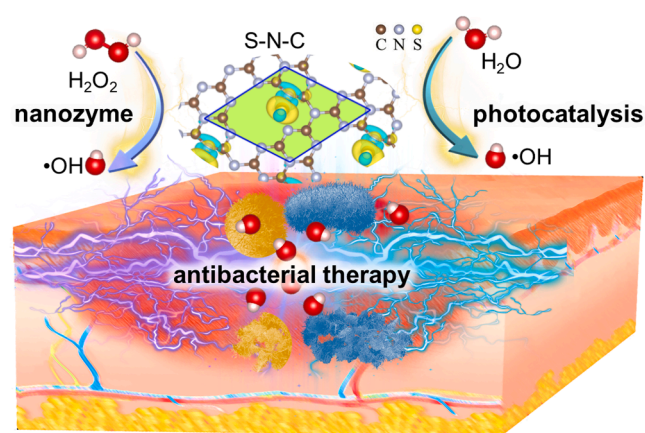
Scheme 1. Schematic diagram of photocatalysis and enzyme synergistic antibacterial therapy.

systems which can achieve efficient space charge separation for water purification [49,50]. Up to now, there is no report on the application of g-CN based materials for boosting bacteria-killing by synergistic effect of photocatalysis and nanozyme.

Inspired by these studies, porous g-SCN nanosheets were prepared by a one-pot copolymerization process through employing thioacetamide as the sulfur source. Density functional theory (DFT) computation and experimental identified that g-SCN has the enhanced photocatalytic and nanozyme catalytic activity. Moreover, we disclose that the active site of the nanozyme is derived from S-N-C coordination by establishing different models. The specific surface area of the composite structure can reach 68.4 m^2g^{-1} ascribed to the porous structure, which is not only exposes more catalytically active sites, but also increases direct contact with bacteria. Under the synergistic effect of photocatalysis and nanozyme catalysis by g-SCN, it has stronger bactericidal properties can kill gram-negative bacterium Chl^r *E. Coli* and gram-positive bacterium MRSA with an antibacterial efficiency up to 100% in 30 min. Our results open the door to the design of g-CN based nanomaterials with high photocatalysis and nanozyme catalysis activity for alternative antibiotics antibacterial therapy (Scheme 1).

2. Experimental section

2.1. Sample preparation

2.1.1. Preparation of g-CN

10 g urea was loaded into porcelain crucible then calcined at 600 °C in a muffle furnace kept for 3 h with healing rate 0.5 °C/min. The obtained product was ground to a homogeneous powder and denoted as g-CN. After heating, the resulting product was gently grounded and treated under ultrasonication for 3 h as an aqueous solution (1 g mL^{-1}). Then the powder was filtered, washed, and dried at 80 °C for further tests.

2.1.2. Preparation of g-SCN

g-SCN was synthesized by similar procedure to g-CN, but the proper amount (1.43 g, 2.00 g, 3.34 g, 10.00 g) of was mixed with thioacetamide and urea together before calcination process. After heating, the resulting product was gently grounded and treated under ultrasonication for 3 h as an aqueous solution (1 g mL^{-1}). Then the powder was filtered, washed, and dried at 80 °C for further tests. The as-synthesized products with different adding amount of thioacetamide were labeled as g-SCN-1, g-SCN-2, g-SCN-3 and g-SCN-4 respectively.

2.2. POD-like activity of g-SCN

The peroxidase-like activity assays of g-SCN were carried out using 3,3′,5,5′-tetramethylbenzidin (TMB) as the substrate in the presence of H_2O_2 in acetic acid buffer. The absorbance of the color reaction (at 650 nm for TMB) was recorded at a certain reaction time *via* a UH4150 (Hitachi) UV-Vis spectrophotometer to express the POD-like activity. Typically, chemicals were added into 1.0 mL acetic acid buffer in an order of certain amounts of the g-SCN. 20 μL TMB (final concentration 40 mM), and 20 μL H_2O_2 (final concentration 1 M) to show the chromogenic reactions implying POD-like activity. The steady-state kinetic assays were conducted at 25 °C in a 1 mL acetic acid buffer with different amounts (0, 20, 40, 60, 100, 200 μL) of g-SCN solution (1 mg mL^{-1}) as catalyst in the presence of H_2O_2 and TMB. The kinetic assays of g-SCN with TMB as the substrate were performed by adding 20 μL 1 M H_2O_2 and different amounts (0, 10, 20, 50, 100, 200 μL) of TMB solution (in DMSO, 40 mM). The kinetic assays of g-SCN with H_2O_2 as the substrate were performed by adding 20 μL of 40 mM TMB and different amounts (0, 5, 10, 15, 20, 25, 30,50, 100 μL) of 1 M H_2O_2 solution. The pH dependence of the POD-like activity of g-SCN was detected in different buffer solutions with pH values from 1.7 to 6. All reactions were monitored by measuring the absorbance at unified reaction times.

2.3. Mechanism of •OH produced by the photocatalysis

The g-SCN can absorb light from the UV to NIR region and produce electrons (e^-) and holes (h^+), which can further react with H_2O to produce •OH. The reactions are listed in Eq. (1)-(2) [51].

$$g - SCN + 2hv \rightarrow g - SCN + 2h^+ + 2e^- \tag{1}$$

$$2H_2O + 2h^+ \rightarrow 2 \cdot OH + 2H^+ \tag{2}$$
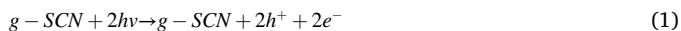
2.4. Antibacterial performance

In this experiment, all culture medium (Luria-Bertani (LB) medium) solution and apparatuses were sterile. Chl^r *E. coli* and Methicillin-resistant Staphylococcus aureus (MRSA) were used as the model of bacterium strains. The bacteria were grown on LB agar plate were transferred to 50 mL of LB at 37 °C and shaken for 12 h, respectively. Bacteria were harvested by centrifuging (8000 rpm for 5 min), and then were washed with deionized water for three times. The supernatant was discarded and the remaining bacteria were resuspended in sterilized saline solution. And then the sample was leaded to $1 * 10^5$ colony forming units (CFU)/mL *via* serially diluting with sterilized saline solution. Take 40 μL of g-SCN solution (1 mg mL^{-1}), 20 μL bacterial liquid (CFU/mL) and 20 μL1M H_2O_2 were dispersed in 1 mL acetic acid buffer (pH = 6), and then exposed to a Xe lamp (300 W) equipped with a AM 1.5 filter. The near-infrared light (NIR) was irradiated by the xenon lamp used above which further equipped with NIR filter (λ > 700 nm). The group of only light without materials as a comparison. The bacterial concentration was measured using standard spread-plating techniques. 100 μL of the bacterial solution from all groups was applied to the LB plate, and after 16 h of growth, the number of single colonies was counted.

2.5. Morphology observation of bacteria

After the antibacterial abilities assessment, three typical groups of the bacterial suspensions (a) acetic acid buffer, (b) H_2O_2 + light (20 μM), (c) H_2O_2 + g-SCN + light (40 μg mL^{-1}), fixed with 4% para-formaldehyde containing phosphate buffer saline (PBS) solution for 4 h at 4 °C. Then, the bacteria were dehydrated by sequential treatments with 10%, 30%, 50%, 70%, 90%, and 100% of ethanol, respectively, for 30 min. Dried bacteria to get SEM images.

2.6. In vivo antibacterial activity and wound healing

Balb/c mice (female, 6 weeks, 18–20 g body weight) were obtained from Vital River Corp. Beijing. The animals were kept in an environment complying with the NIH guidelines for the care and use of laboratory animals. All animal experiments were conducted using protocols approved by the Institutional Animal Care and Use Committee at the Institute of Tumors at the Chinese Academy of Medical Sciences (11040202450060). The dorsal hair of mice was shaved and the animals were anesthetized by intraperitoneal (i.p.) injection of pentobarbital sodium with a dose of 40 mg kg^{-1} body weight. A rounded full-thickness skin wound (~5 mm × 5 mm) was created by excising the dorsum of the animals on the backside. The wounds were infected with 10 μL (10^6 CFU mL^{-1}) MRSA and bandaged with elastic bandages. Twenty-four hours later, the mice were divided into eight groups and four mice (n = 4) for each group and treated with synergistic therapy of photocatalysis and nanozyme catalysis. The MRSA infected wound was treated with PBS, g-SCN, light, H_2O_2 + light, g-CN + H_2O_2 + light, g-SCN + H_2O_2, g-SCN + light, g-SCN + H_2O_2 + light, respectively. The final concentration is g-CN and g-SCN: 1 mg mL^{-1}, H_2O_2: 50 μM. For the light treatment group, a xenon lamp equipped with AM 1.5 G filter (100 mW/cm^2) was used as the light source. The irradiation time is 30 min. Then, the animals were individually housed in cages and allowed to heal. The body weight and wound size of the animals were recorded daily. At the termination of the experiments, the animals were sacrificed. The skin tissues of the wound regions were retrieved. The tissues were fixed in 10% formalin, embedded in paraffin, sectioned in 8 μm thick sections, and used for hematoxylin and eosin (H&E) staining and Masson's trichrome staining for histological examination using standard techniques.
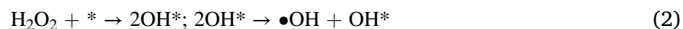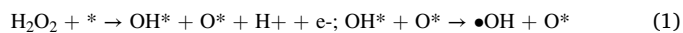
2.7. Statistics

The results are expressed as mean $\pm$ standard deviation. Standard deviation is indicated by the error bars. Student's t-test was used to determine significance among the small groups.

2.8. Method and computational details

The first-principles calculations within DFT were implemented by the Vienna *ab-initio* Simulation Package (VASP). A generalized gradient approximation (GGA) in the form of Perdew-Burke-Ernzerhof (PBE) was adopted to describe the electron-electron interactions. The energy cut-off employed for plane-wave expansion of electron wavefunctions was set to 500 eV and the electron-ion interactions were treated using projector-augmented-wave (PAW) potentials. The DFT-D3 method was applied to include the long-range van der Waals interaction for the adsorption on substrate lattices. The vacuum region of about 20 Å was applied along the z-direction to avoid mirror interaction between neighboring images. Structural optimization was carried out using a conjugate gradient (CG) method until the remaining force on each atom is less than 0.05 eV/Å.

Generally, the peroxidase degradation mechanism pathways are generally the following Eq. 1 and 2, respectively.

$$H_2O_2 + * \rightarrow OH^* + O^* + H^+ + e^-; OH^* + O^* \rightarrow \bullet OH + O^* \tag{1}$$

$$H_2O_2 + * \rightarrow 2OH^*; 2OH^* \rightarrow \bullet OH + OH^* \tag{2}$$

where * denotes the corresponding catalyst (g-CN without and with S doping).

To investigate the interaction between the intermediates (H_2O_2, -OH, -O and $-2OH$) and the corresponding substrates, the adsorption energy was defined as the following:

$$E_{ads} = E_{(sub+im)} - E_{(sub)} - E_{(im)}$$

where $E_{(sub+im)}$, $E_{(sub)}$ and $E_{(im)}$ correspond to the total energies of
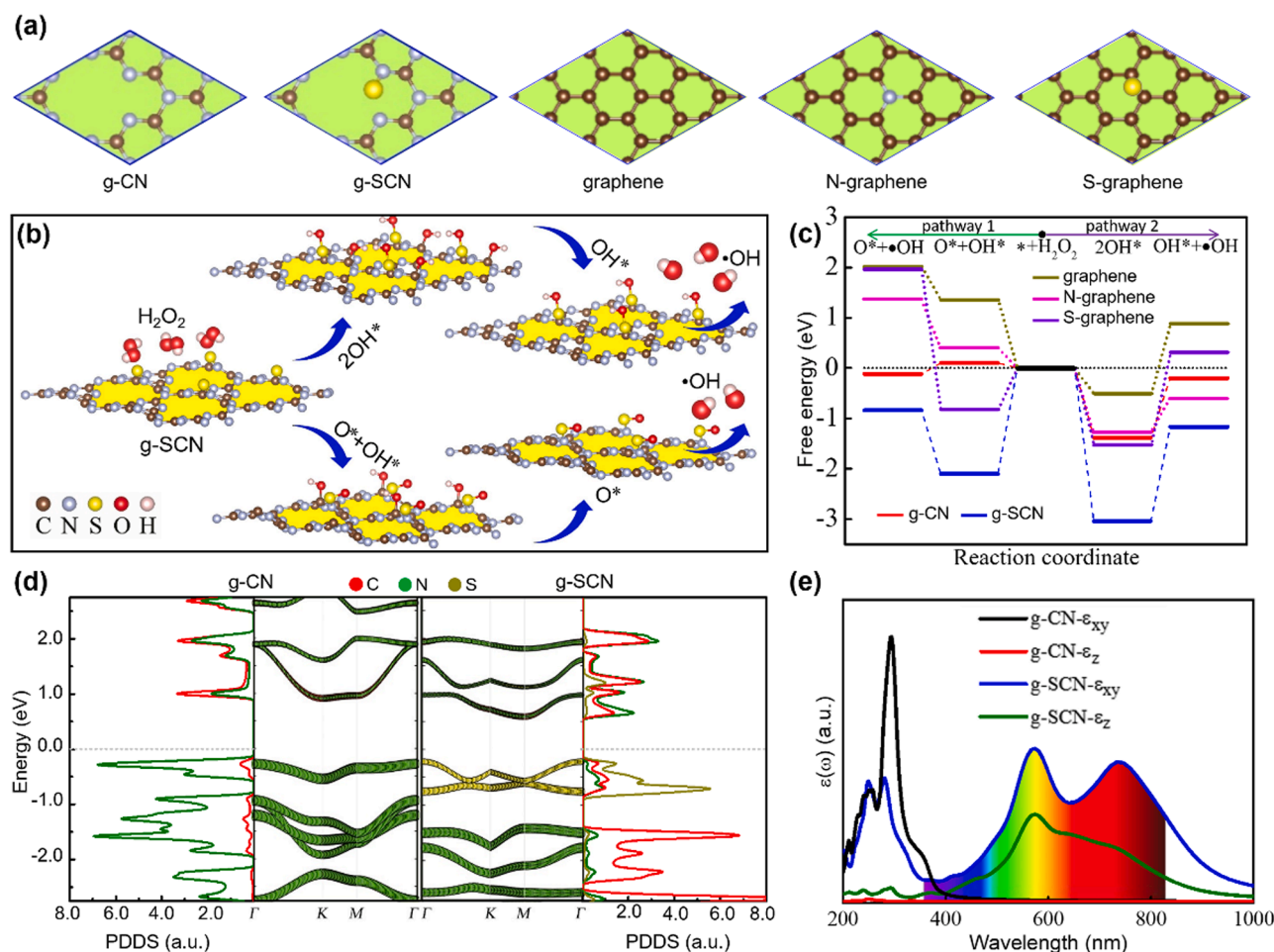
Fig. 1. (a) Schematic illustrations of different models: g-CN, g-SCN, graphene, N-graphene, S-graphene. (b) The intermediates during H_2O_2 decomposition process. (c) The free energy diagrams of the different models for the production of catalyst hydroxyl radical. (d) Orbital-resolved band structures of g-CN and g-SCN lattices. The red, green and yellow dots represent the contributions from C, N and S atoms. The energy at the Fermi level was set to zero. (e) Imaginary parts of dielectric constant for g-CN and g-SCN, respectively.

substrates and intermediates, an isolated substrates and intermediates, respectively. Meanwhile, under standard conditions, the total energies of $H^+ + e^-$ and $1/2\ H_2$ (gas) are equal. A negative value suggests a strong chemisorption as well as the spontaneous exothermic process for the reaction.

We also analyze the charge transfer for those O* +OH* and 2OH* lattices, which is defined as $\Delta Q = Q_{(sub+ im)} - Q_{(sub)} - Q_{(im)}$, where Q $_{(sub+ im)}$, $Q_{(sub)}$ and $Q_{(im)}$ are the charge densities of the corresponding Graphene/N-Graphene systems with intermediate adsorbed, the clean corresponding Graphene/N-Graphene systems and intermediate systems, respectively. As Fig. S1, S2 and S3 shown, charges are transferred from the Mo and S into the surrounding adsorbed intermediates peroxidase degradation, which provides a favorable place for the degradation of hydrogen peroxide.

3. Results and discussion

3.1. DFT calculation

Firstly, we explored the source of nanozyme activity. In order to determine whether the POD-like activity comes from C-S, C-N, or C-N-S coordination, different models were built (Fig. 1a): g-CN, g-SCN, graphene, nitrogen doped graphene (N-graphene), sulfur doped graphene (S-graphene). S atom doping can cause a restructuration of configuration and redistribution of electrons in g-SCN. According to first-principles calculations, quantitatively, the Bader charge analysis

reveals that the S atom has a net diminution of 0.70*e* to the circumferent atoms, while, the N atom (connected with S atom) has a net gain of 0.22*e* from the circumferent atoms (Fig. S1), demonstrating a splendid H_2O_2 decomposition potential performance. In order to investigate the mechanism of POD-like activity, typical models of g-SCN (Fig. 1b and S2) were built to explore H_2O_2 activation process. Then the adsorption energies of intermediate products during H_2O_2 decomposition process were calculated. In addition, the reactions of g-CN, graphene, N-graphene, and S-graphene surface were also given here as a benchmark (Fig. S3-S9). Fig. 1c displayed that in pathway 2 the intermediate 2OH had negative adsorption energies in both g-CN and g-SCN models, indicating stable adsorption. The 2OH adsorption in g-SCN lattice was the most stable states owing to the extremely large values − 0.20 eV/ atom, implies that the •OH desorbed in g-SCN lattice would easily proceed with the larger exothermic process. Although g-CN lattice spontaneously adsorbed the intermediate 2OH, the free energy (−0.10 eV/atom) is not big enough to overcome the decisive step of •OH decomposition (0.08 eV/atom). Furthermore, it was also exhibited the free energy diagrams of g-CN and g-SCN lattice under the condition of pathway 1. Obviously, the •OH desorbed under the condition of pathway 1 could happen spontaneously from an energy perspective in both cases, due to the exothermic reaction with values of − 0.01 eV and − 0.06 eV/atom in the whole process. However, smaller exothermic energies indicate the relatively slow reaction rates. Especially, the O-OH adsorption in g-CN lattice is an endothermic reaction, which would have greatly hindered the reaction going forward. From the first principle
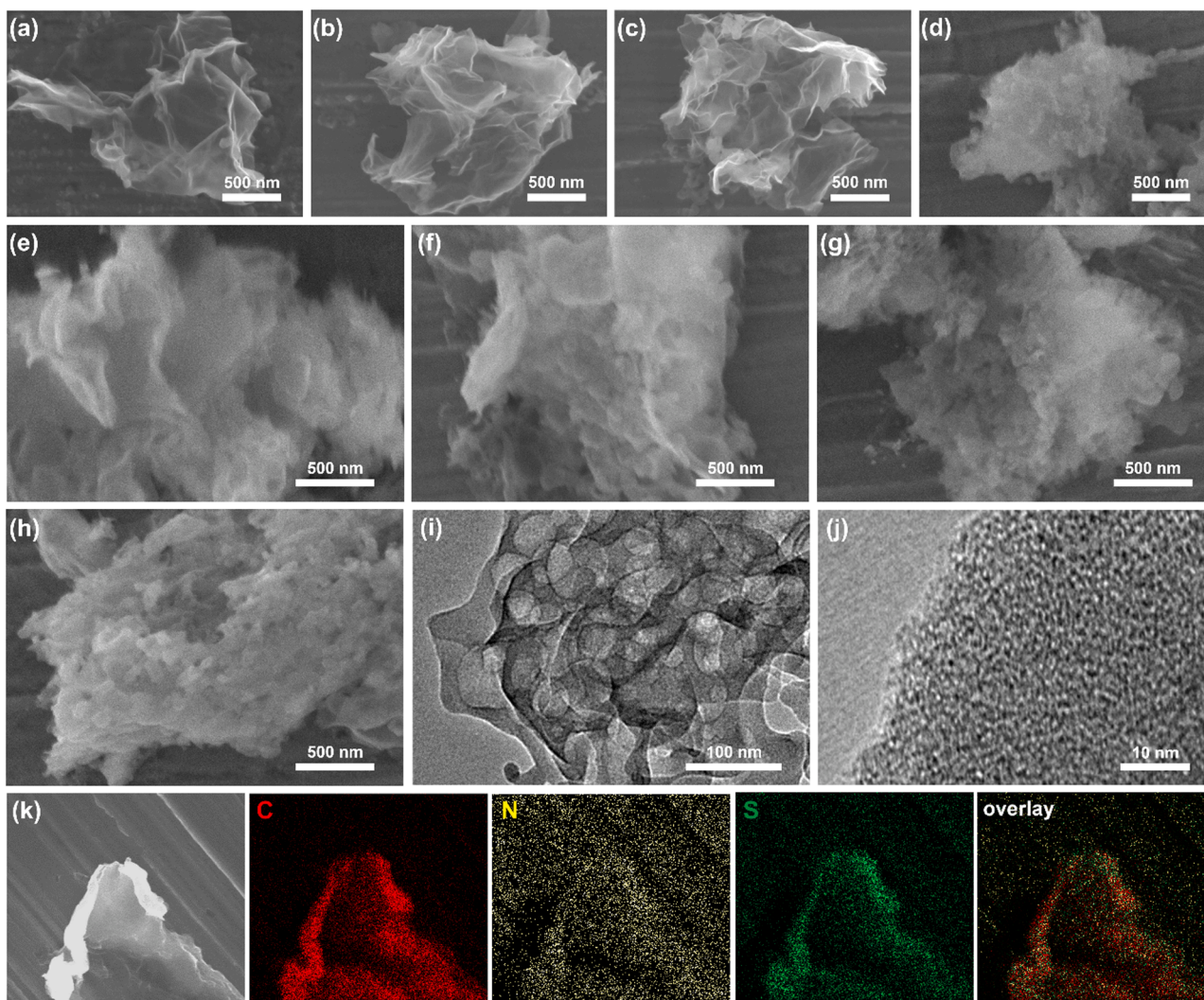
Fig. 2. SEM images of the different samples: (a) rGO, (b) N-rGO, (c) S-rGO, (d) g-CN, (e-h) g-SCN with different S doping concentration. (i) TEM and (j) HRTEM images of g-SCN. (k) SEM image and the corresponding C, N and S elements mapping of g-SCN.

calculation, it could be seen that S doping endows g-CN POD-like activity.

Alternatively, the restructuration of configuration also could induce the novel electronic properties and even novel optical properties. Both the valence band maximum (VBM) and conduction band minimum (CBM) of g-SCN moved towards Fermi surface in different degrees compared with g-CN as shown in Fig. 1d. The orbital-resolved band structures indicated that the CBM is from the contributions of the p_z-orbital of C atoms, while, the VBM is composed mainly of the p_{xy}-orbital of S, which will lead to novel optical phenomena.

The optical absorption properties were investigated by computing the complex dielectric function, $\varepsilon(\omega) = \varepsilon_1(\omega) + i\varepsilon_2(\omega)$, in which the imaginary part $\varepsilon_2(\omega)$ reflects optical absorption at a given frequency ω. The imaginary part $\varepsilon_2(\omega)$ can be written as:

$$\varepsilon_{\alpha\beta}(\omega) = \frac{4\Pi^2 e^2}{\Omega} \lim_{q \to 0} \frac{1}{q^2} \sum_{c,v,\vec{k}} 2w_{\vec{k}} \delta\left(\varepsilon_{\overrightarrow{ck}} - \varepsilon_{\overrightarrow{vk}} - \omega\right)$$
$$\times \left\langle u_{\overrightarrow{ck}+e\alpha q} \middle| u_{\overrightarrow{vk}} \right\rangle \left\langle u_{\overrightarrow{ck}+e\beta q} \middle| u_{\overrightarrow{vk}} \right\rangle^*$$

The knowledge of $\varepsilon_2(\omega)$ over a wide frequency range allows one to obtain $\varepsilon_1(\omega)$ using the Kramers-Kronig relation. The $\varepsilon_2(\omega)$ decomposed into two components $(\varepsilon_{xx} + \varepsilon_{yy})/2$ and ε_{zz}, marked as ε_{xy} and ε_z (as shown in Fig. 1e), which correspond to the electric field polarization perpendicular and along to the hexagonal system z-direction, respectively. Taking S into account, a significant absorption spectrum along xy-direction in the visible and near infrared regions, which ranges from 400 nm to 1000 nm. Meanwhile, S also can strong contribute the visible light absorption in the z-direction. Except the visible light, there is an obvious absorption peak in the infrared region, ranging from 780 nm to 900 nm, which greatly affects the light absorption characteristics of g-SCN.

3.2. Morphology and crystal structure of the catalysts

Under the guidance of DFT theory, the different models' samples were successfully synthesized. Fig. 2a-h show the scanning electron microscope (SEM) images of the different samples: rGO, N-rGO, S-rGO, g-CN, and g-SCN with different S doping concentration. The basic unit of g-CN is ultrathin nanosheet with a lateral scale of several micrometers, similar to the graphene nanosheet. After S doping, the surface morphologies of different S doping concentration has no obvious change. Furthermore, the morphologies were also characterized using transmission electron microscope (TEM). Many small holes (diameter about 50–60 nm) on the surface were observed on the g-SCN (Fig. 2i) compared to the g-CN. This may be caused by the introduction of thioacetamide in the thermal polycondensation process, which destroy the polycondensation process. Furthermore, g-CN is prepared by thermal
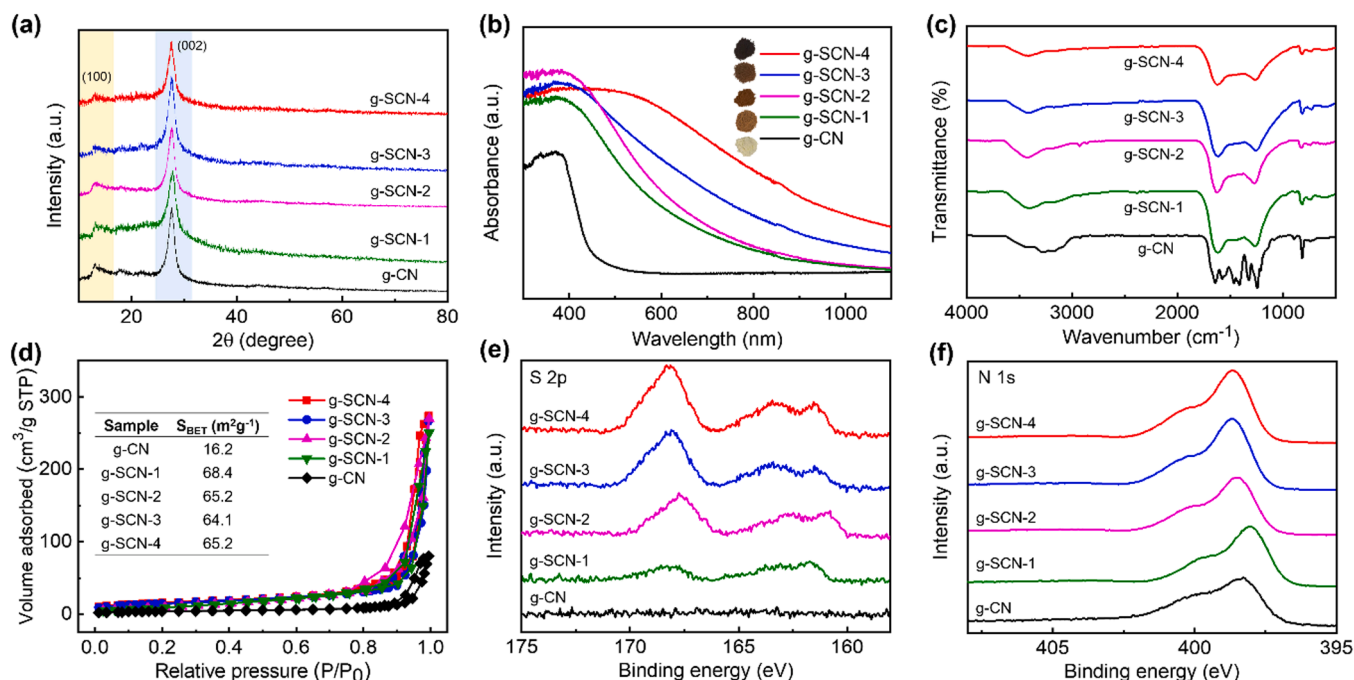
Fig. 3. (a) XRD patterns, (b) UV–vis diffuse reflectance spectra. (c) FTIR spectra, (d) N$_2$ adsorption-desorption isotherms, and high-resolution XPS spectrum of (e) S 2p and (f) N 1 s of g-CN and g-SCN with different S doping concentration.

urea of carbon and nitrogen containing monomers at elevated temperatures. The urea process is hindered at later stages by the sluggish deamination kinetics and thus generates PCN with incomplete condensation and lower local order. So the crystallinity is poor [52]. Due to the poor crystallinity, we did not observe a distinct lattice structure in the high resolution TEM (HRTEM) image of g-SCN (Fig. 2j). In order to prove S doping, we characterized it by element mapping. As displayed in Fig. 2k, S elements are evenly distributed in g-SCN.

The crystal structure of the samples was then characterized by X-ray diffraction (XRD) patterns (Fig. 3a). The XRD pattern of g-CN shows two characteristic peaks at 13.0° and 27.4°, which can be assigned to the intralayer repeated packing heptazine units (100) and interlayer stacking (002) of g-CN (JCPDS 87–1526), respectively [53]. For g-SCN samples, a gradual weakening can be observed on both the two characteristic peaks with the increasing calcination temperature, indicating that the addition of S atoms caused the loss of ordered structures within the framework [54,55]. The optical properties of the materials were studied by recording UV–vis diffuse reflectance spectra (Fig. 3b). The absorption intensity of pure g-CN was observed in the range of visible light. The absorption cutoff edges are about 450 nm. With the increase of the S element doping, the absorption in the visible light range accordingly increases, which is beneficial for the efficient use of solar light in a wider spectra range. It is consistent with our results calculated by DFT (Fig. 1e).

The Fourier transform infrared spectroscopy (FTIR) spectrum for g-CN (Fig. 3c) show a peak at 803 cm^{-1} originating from the out-of-plane bending mode of triazine unit. The peaks in the range of 1200–1700 cm^{-1} correspond to the stretching modes of aromatic C-N heterocycles. Multiple broad peaks locating between 3000 and 3500 cm^{-1} were typically for N-H stretching vibrations. Due to the introduction of S element, which could form coordination with N atom. So, the peaks of N-C and N-H change slightly. Furthermore, it is important that high surface area in promoting the antibacterial performance of g-SCN. The high surface area could provide more active sites and improve the contact area between bacteria and materials [56]. As shown in Fig. 3d, N$_2$ sorption isotherms of the g-SCN show presentative type-IV curve with a typical H3-type hysteresis loop, which indicates the highly porous structure. As expected, g-SCN with different S doping has

larger specific surface areas (68.4, 65.2, 64.1 and 65.2 m^{2}g^{-1} respectively) than pure g-CN (16.2 m^{2}g^{-1}).

The chemical composition and valence state were characterized by X-ray photoelectron spectroscopy (XPS) (Fig. S15 show the full survey spectrum). Fig. 3e is the high-resolution XPS spectrum of S 2p. Since pure g-CN does not contain S, no signal of S species can be detected. With the increase of S doping, the peak intensity increases gradually. N 1 s spectrums of the samples are displayed in Fig. 3f, the peak shape does not change significantly with the increase of sulfur doping concentration.

3.3. Bactericidal mechanism

By measuring their POD-like activity (Fig. 4a), it could be seen that compared with rGO, S-rGO showed no POD-like activity, and N-rGO showed slightly improved POD-like activity. It was evident that neither C-S nor C-N bond is the main source of nanozyme activity. This also confirms our conjecture that the coordination of C-N-S in g-SCN is the key to affect nanozyme activity. For the g-SCN, the absorbance of TMB oxidation product (oxTMB) at 652 nm is increased with time in the mixture of H$_2$O$_2$, TMB and g-SCN, shown the highest POD-like activity. As displayed in the Fig. 4b, the absorbance of oxTMB is increased with time. And the g-SCN-2 (In this paper, g-SCN is used instead of g-SCN-2 unless otherwise specified) shown the highest POD-like activity. Similar to natural enzyme, the substrate concentration, pH and temperature will also affect the enzymatic reaction rate. The enzymatic reaction rate was directly ratio to H$_2$O$_2$ (Fig. 4c), and the optimum pH was 3.6 (ranging from 1.6 to 6.0) and the optimum reaction temperature was 40 °C (ranging from 25° to 60°C) (Fig. 4d). Furthermore, the stability and repeatability of g-SCN was also determined. It shows that after 50 reaction cycles, the performance can still maintain more than 85% (Fig. S16). The crystal structure (Fig. S17), surface morphology (Fig. S18) and constituent elements (Fig. S19) also did not change significantly. From the XPS results (Fig. S20 and S21), the surface of the material still contains C, N and S elements, and the peak of S element has no obvious change. It is suggested that the molecular structure of nanozyme does not change before and after the POD-like catalytic behavior.
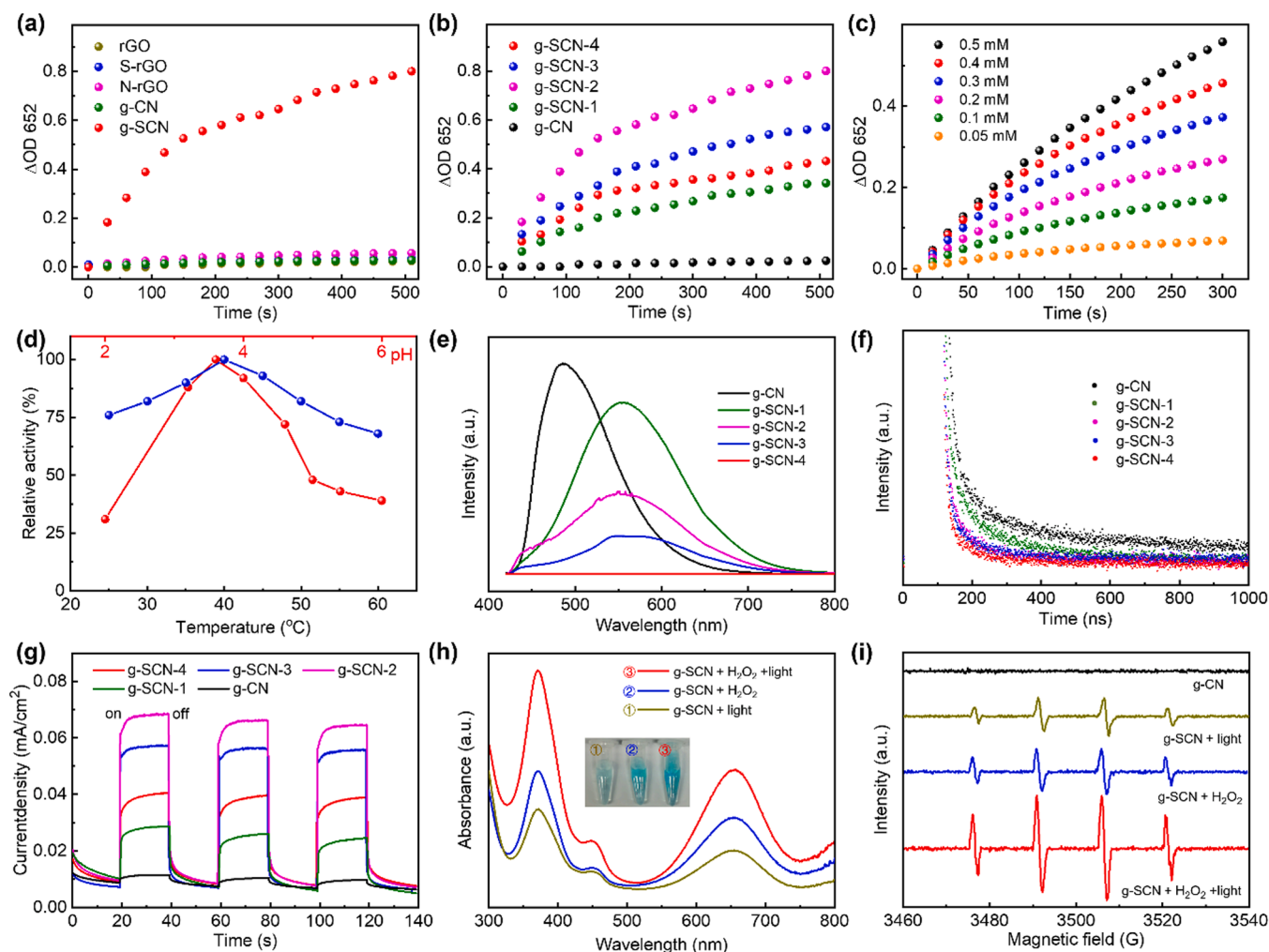
Fig. 4. (a) Time-dependent absorbance of oxTMB for the different samples. (b) Time-dependent absorbance of oxTMB: g-SCN with different S doping concentration. Concentration: g-SCN 40 μg mL^{-1}, H_2O_2 2 mM, TMB 800 μM. (c) Time-dependent absorbance of oxTMB: g-SCN-2 with different H_2O_2 concentrations. (d) pH and temperature-depended POD-like activity of g-SCN-2. (e) Steady-state PL spectra. (f) TRPL decay curves. (g) Photocurrent density of g-SCN nanosheet with different S doping concentration. (h) Typical UV–vis spectra and visual color change of TMB in different systems. 1, g-SCN + light; 2, g-SCN + H_2O_2; 3, g-SCN + light + H_2O_2. (i) •OH detection by using EPR spectra.

Sulfur doping can not only endow g-SCN POD-like activity, but also enhance its original photocatalytic performance. The broadening of the absorption spectrum of the g-SCN can enhance the generation of carriers. To gain in-depth insights of the charge separation efficiency in g-SCN by the introduction of S doped, the steady-state photoluminescence (PL) spectra and time resolved PL (TRPL) decay spectra of samples were conducted [57]. In comparison, the PL spectra for fluorescence intensity decreases with the increase of S doping concentration (Fig. 4e), indicating the significantly suppressed electron-hole recombination. In order to track the charge transport dynamics in real time, the lifetime of g-SCN is longer than that of through fitting of the TRPL spectra (Fig. 4 f), indicating the lowest charge carrier recombination rate for g-SCN. To further explain the enhancement of the photocatalytic property of the g-SCN, the photocurrent performance of the materials was measured. As can be seen from Fig. 4 g, the g-CN exhibits negligible photocurrent, only 0.013 mA cm^{-2}. The photocurrent densities of the g-SCN-1 and g-SCN-4 are about 0.027 and 0.038 mA cm^{-2}, while the photocurrent of the g-SCN-2 and g-SCN-3 photoanode approaches 0.068 and 0.056 mA cm^{-2}, which more than 5.2 and 4.3 times higher than pristine g-CN, respectively.

Hydroxyl radical (•OH), which is the strongest oxidant known, can quickly decompose the RNA, enzymes, lysozyme and other substances contained in microorganism, so as to achieve the effect of sterilization

and disinfection [58–60]. Therefore, the production of •OH is very important to the bactericidal effect. The production of •OH was measured by TMB oxidation method. It can be seen from the Fig. 4 h, •OH can be produced only by photocatalysis (curve 1) or nanozyme catalysis (curve 2). When both of them act together, the yield of •OH increases nonlinearly (curve 3), which can be increased rapidly, higher than the sum of the two. Moreover, the produced •OH was also detected by electron paramagnetic resonance (EPR). As presented in Fig. 4i, when H_2O_2 is added or light applied to the g-SCN/DMPO system, a typical •OH signal peak appears in the EPR spectrum. The results prove that •OH can be produced in photocatalytic or enzymatic reaction system. When the two effects cooperate, the signal of •OH is further improved. Moreover, we compared the combination index (CI) values of the g-SCN + light, g-SCN+ H_2O_2, and g-SCN + H_2O_2 + light (Fig. S22). It showed that all the CI values of the g-SCN + light + H_2O_2 were lower than 1, which demonstrates a strong synergy. From the above results, it confirmed that g-SCN is both a nanozyme catalyst and a photocatalyst, which can generate •OH storm in the corresponding substrate.

3.4. Photocatalytic disinfection performance in vitro

The antibacterial ability of chloramphenicol-resistant Gram-negative *E. coli* (Chl^r *E. coli*) and gram-positive bacterium Methicillin-resistant
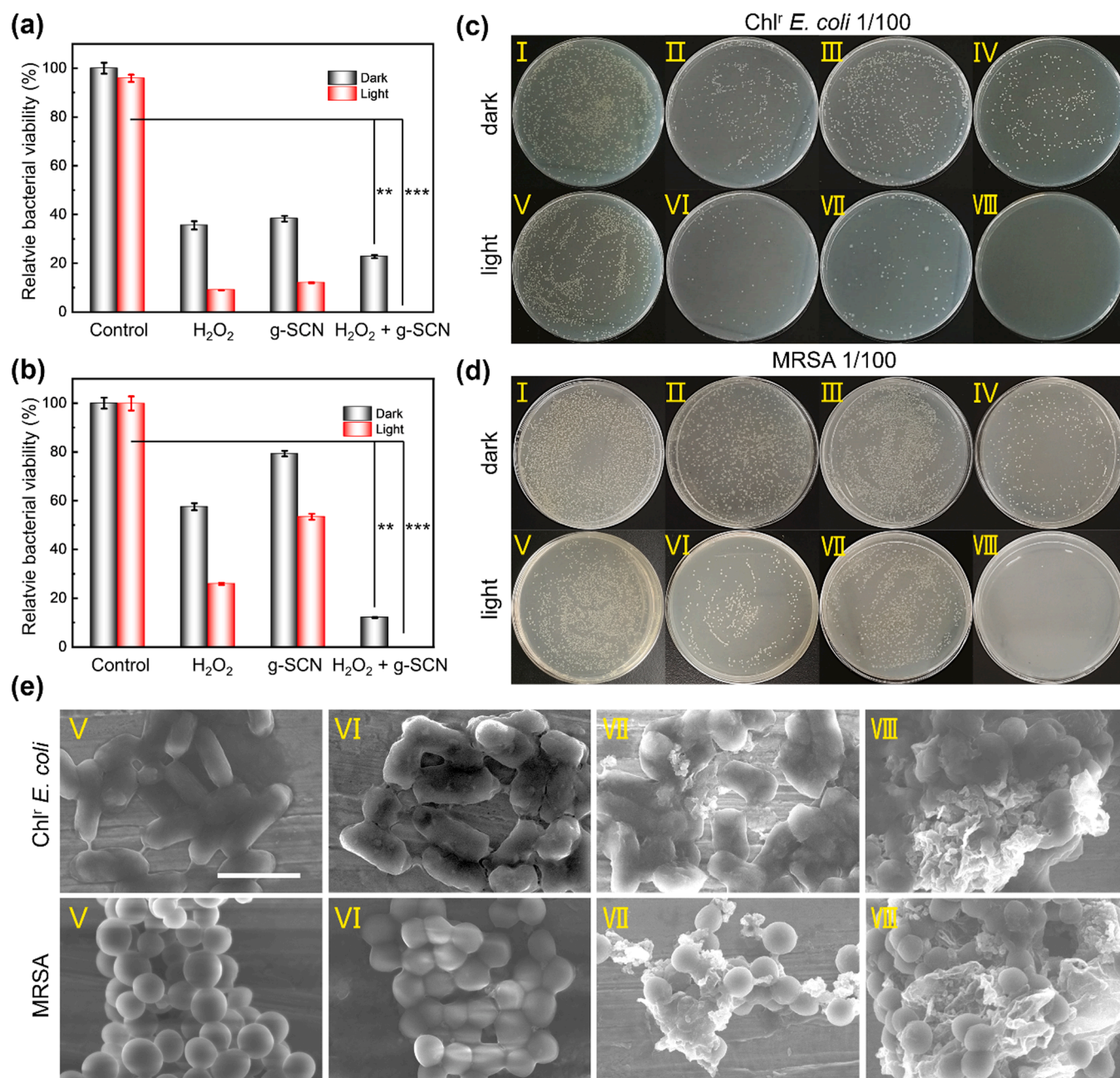
Fig. 5. (a, b) Relative survival rate of bacteria for Chl^r *E. coli* (a) and MRSA (b) determined by plate count method under different conditions: (I) control, (II) H$_2$O$_2$, (III) g-SCN, (IV) g-SCN + H$_2$O$_2$, (V) control + light, (VI) H$_2$O$_2$ + light, (VII) g-SCN + light, and (VIII) g-SCN + H$_2$O$_2$ + light. Concentration: H$_2$O$_2$ 50 μM, g-SCN 100 μg mL^{-1}. **p < 0.01, ***p < 0.001. (c, d) Photographs of bacterial colonies: (c) Chl^r *E. coli*, (d) MRSA. (e) The corresponding SEM images of bacteria.

Staphylococcus aureus (MRSA) were examined by classical plate count method (Fig. 5a and b). Through the comparison of eight groups: I) control, II) H$_2$O$_2$, III) g-SCN, IV) g-SCN + H$_2$O$_2$, V) control + light, VI) H$_2$O$_2$ + light, VII) g-SCN + light, and VIII) g-SCN + H$_2$O$_2$ + light, group VIII shows relatively the highest antibacterial activity, owing to the photocatalysis and nanozyme catalysis of g-SCN synergistically to generate more •OH, which extremely efficient bacterial killing (an inhibition rate of up to near 100%) both on Chl^r *E. coli* and MRSA. The antibacterial effect of different materials can also be seen more intuitively from the bacterial culture. The eighth group basically has no growth of bacterial colonies for Chl^r *E. coli* (Fig. 5c) and MRSA (Fig. 5d). To further decipher the antibacterial behavior, the morphologies of the bacterial were measured by SEM. As shown in Fig. 5e, the bacteria show uniform size (Chl^r *E. coli* is rod-shaped and MRSA is sphere-shaped) smooth surface and intact membrane in the control group. After

treatment with H$_2$O$_2$ (VI) or g-SCN + light (VII) for 50 min, a few disruptions could be identified on cell walls, which indicated that H$_2$O$_2$ or g-SCN + light alone only have limited influence on the integrity of cell walls. After treatment with (VIII) g-SCN + H$_2$O$_2$ + light for 50 min, the cell walls combined with g-SCN closely and became strong wrinkled and incomplete. It is point to the fact that this synergistic system possesses a stronger antibacterial ability. In addition, g-SCN also had bactericidal properties against Chlr *E. coli* under NIR light (Fig. S23). It could kill 95% of Chl^r *E. coli* and 85% of MRSA within 90 min

3.5. Antibacterial photocatalytic therapy

It has been reported that glutathione (GSH) played an important role in the bacterial antioxidant defense system, which can prevent damage to cellular components induced by oxidative stress, and it has been acted
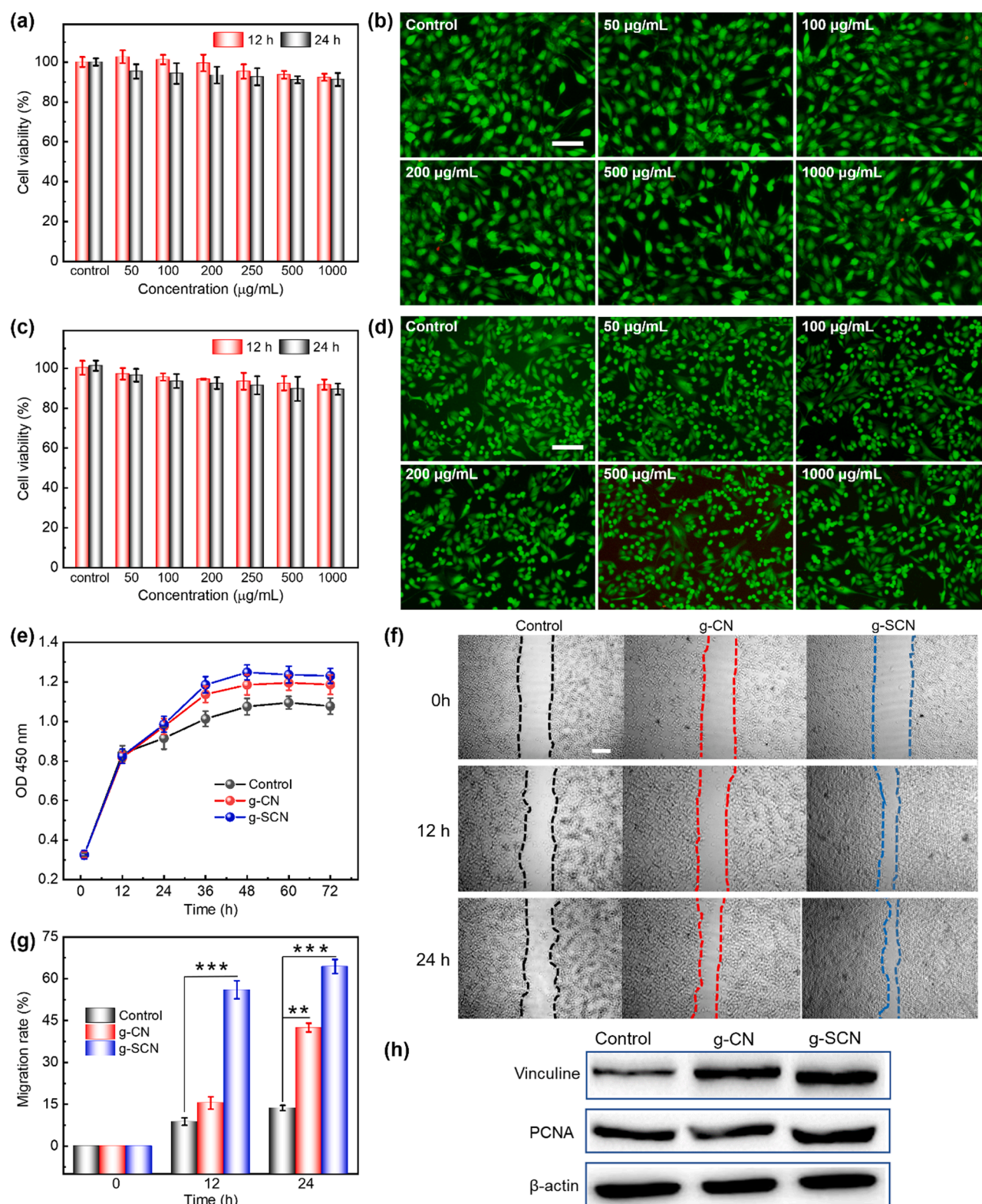
Fig. 6. Cytotoxicity of g-SCN in (a, b) 3T3 and (c, d) HSF cells. (a, c) Cell viability with CCK-8 assay. (b, d) Live/dead cell staining at 24 h. The scale bars in (b) and (d) are 100 μm. (e) Effect of different materials on the proliferative capacity of HSF cells. (f) Representative images of HSF cell migration from the scratch healing assay at different times. The scale bars are 200 μm. (g) Migration rate of HSF cells in different material groups. **p < 0.01, ***p < 0.001. (h) Expression of related proteins in HSF cells after treatment with different materials.
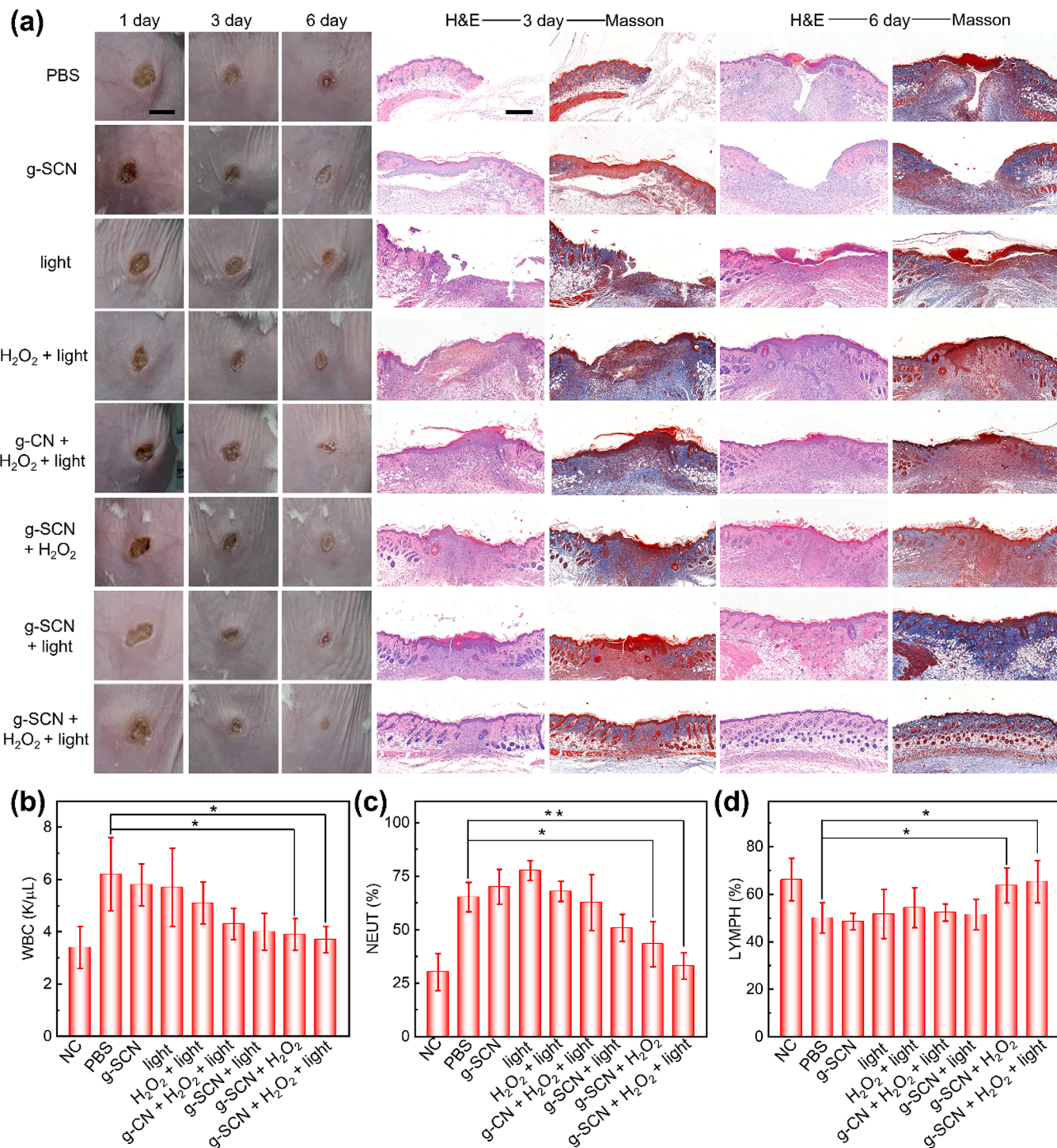
Fig. 7. (a) Photographs of infected wound treated in different days (1, 3, 6) and the pictures of histologic analyses in different days (3, 6) with different treatments: PBS, g-SCN, light, H_2O_2 + light, g-CN + H_2O_2 + light, g-SCN $_2O_2$, g-SCN + H+ H_2O_2, g-SCN + H+ H_2O_2 + light. The scale bars are 0.5 cm and 400 μm in the photographs and histologic pictures, respectively. The routined blood test after different treatments: (b) WBC number, (c) NEUT ratio, and (d) LYMPH ratio. *p < 0.05, **p < 0.01.

as oxidative stress indicator in cells. To investigate oxidative stress induced by g-SCN, Ellman's assay was employed to measure the GSH oxidation. As shown in the Fig. S24, the loss of GSH in the dark was attributed to the oxidative lesions of g-SCN. The loss of GSH can reach 55% in 10 min and then remains essentially unchanged. Typically, after incubation with GSH, g-SCN show a time-dependent oxidation behavior. The statistical loss of GSH can reach to almost 100% after addition of g-SCN for 60 min under light irradiation.

To further examined the biocompatibility of g-SCN, 3T3 and human skin fibroblasts (HSF) cells were co-cultured with g-SCN. First, the toxicity to cells of the as-synthesized g-SCN was evaluated by Cell Count Kit-8 (CCK-8). As shown in Fig. 6a and c, there was almost no decrease in cell activity when the concentration of g-SCN arrived 100 μg mL^{-1}. It remained 95% and 92% at 24 h for 3T3 and HSF cells, respectively. When it arrived 1000 μg mL^{-1} (10 times used for the bactericidal concentration), they also successfully maintained 94% and 90% viability at

24 h. Moreover, in order to denote the live and dead cells, the 3T3 and HSF cells were stained with calcein-AM (green) and EthD-1 (red). It demonstrated that the g-SCN shown no harm to the normal cells (Fig. 6b and d), which shown the potential application in the biological field. The toxicity to normal cells of g-SCN was also evaluated by 3-(4,5-Dimethylthiazol-2-yl)− 2,5diphenyltetrazoliumbromide (MTT). Same as expected, there was almost no significant cytotoxicity when the concentration of g-SCN arrived 100 μg mL^{-1} and maintained 88.56% and 86.17% viability for 24 h when concentrations up to 1000 μg mL^{-1}, respectively, which was very close to the results of the CCK-8 assay (Fig. S25). These results further indicated as-synthesized g-SCN possessed excellent biosafety and was highly suitable for clinical treatment.

As we all known, in the process of skin repair, if enhance the abilities of cell proliferation and migration, could be very conducive to wound healing. Thus, HSF cell was chosen for cell proliferation and migration test *in vitro*. The results are displayed in Fig. 6e-f, both g-CN and g-SCN promoted the cell proliferation and migration of HSF cells at the dose of 100 μg mL^{-1} compared with the control group, signifying that g-SCN have a positive effect on enhancing skin tissue repair. Meanwhile, the expression of the corresponding protein was also up-regulated after western blot detection in Fig. 6 h. The above consequences suggested that g-SCN with great biocompatibility could promote cell proliferation and migration, which may facilitate the repair of damaged tissue.

Considering that g-SCN displayed choice synergistic bactericidal performance, negligible cytotoxicity and the ability to promote cell proliferation and migration, we further evaluated its healing capacity on the infected wounds. Fig. 7a exhibits the wound photographs and corresponding histological analyses results of mice under different treatments: PBS, g-SCN, light, H_2O_2 + light, g-CN + H_2O_2 + light, g-SCN $_2O_2$, g-SCN + H+ H_2O_2, g-SCN + H+ H_2O_2 + light, respectively. On the third day, except the PBS, g-SCN and light groups, the other treatment groups could observe an obvious scar, and the would size was reduced. Meanwhile, the hematoxylin and eosin (H&E) staining and Masson's trichrome staining denote that there was still obvious inflammation at the wound, and the boundary with normal tissue was clear. On the sixth days, the wound size decreased in all treatment groups. The wound for the treatment group of g-SCN + H_2O_2 + light almost disappeared, which also exhibited splendid collagen fibers regeneration and thick dermis. At the same time, the PBS, g-SCN and light groups showed the incomplete dermal layer. In the H_2O_2 + light, g-CN + H_2O_2 + light, g-SCN + H_2O_2, g-SCN + H_2O_2 groups, although the wound tissue is continuous, it still has inflammation, and the wound boundary between normal tissue and the wound could be still observed.

Similarly, the declined rate of the wound area in the g-SCN + H_2O_2 + light group was also the fastest (Fig. S26). The wound area on the sixth day for the different treatment groups PBS, g-SCN, light, H_2O_2 + light, g-CN + H_2O_2 + light, g-SCN $_2O_2$, g-SCN + H+ H_2O_2, g-SCN + H+ H_2O_2 + light, reduced to 6.7%, 28.5%, 32.5%, 46.2%, 59.2%, 68.5%, 70.5% and 73.9%, respectively. Concomitantly, the body weight of wound infected mice gradually recovered, especially in the g-SCN + H_2O_2 + light group (Fig. S27). Moreover, the routine blood test was assessed so as to monitor the systemic inflammatory response in mice. As shown in Table S1 and Fig. 7b-d, g-SCN + H_2O_2 + light group had an apparent antibacterial property due to the white blood cell (WBC), neutrophilic (NEUT) and lymphocyte (LYMPH) ration remarkably drop return to almost normal levels compared with PBS group.

4. Conclusions

In conclusion, we have successfully prepared porous g-SCN nanosheets *via* a polycondensation strategy. The enlarged specific surface area, broadened photoabsorption and enhanced photocarrier separation contribute to the superior photocatalytic performance of g-SCN. Furthermore, it can also as a nanozyme with POD-like activity. More importantly, we have confirmed that S-N-C coordination is the source of POD-like activity through theory and experiment. Under the synergistic effect of photocatalysis and nanozyme, the g-SCN could kill gram-negative bacterium Chl^r *E. coli* and gram-positive bacterium MRSA with an antibacterial efficiency up to 100%. Furthermore, the g-SCN is successfully applied to mice that were treated for wound infection. This work opened promising avenues for combining photocatalysis with nanozyme for antibacterial therapy.

CRediT authorship contribution statement

Longwei Wang: Conceptualization, Data curation, Formal analysis, Investigation, Writing – original draft. **Zhongwei Yang**: Data curation, Writing – review & editing, Conceptualization. **Guoxin Song**: Supervision, Validation. **Zhen You**: Supervision, Validation. **Xiaoyu Zhang**: Supervision, Validation. **Lin Liu**: Investigation. **Jian Zhang**: Data curation, Software, Visualization. **Longhua Ding**: Supervision, Validation. **Na Ren**: Visualization, Investigation. **Aizhu Wang**: Data curation, Software, Visualization, Funding acquisition. **Jing Liu**: Funding acquisition, Resources, Supervision, Writing – review & editing. **Hong Liu**: Funding acquisition, Supervision, Validation. **Xin Yu**: Conceptualization, Funding acquisition, Project administration, Resources, Supervision, Writing – review & editing.

Declaration of Competing Interest

The authors declare that they have no known competing financial interests or personal relationships that could have appeared to influence the work reported in this paper.

Data availability

The authors do not have permission to share data.

Appendix A. Supporting information

Supplementary data associated with this article can be found in the online version at doi:10.1016/j.apcatb.2022.122345.

References

[1] I.E. Mba, E.I. Nweze, Nanoparticles as therapeutic options for treating multidrug-resistant bacteria: research progress, challenges, and prospects, World J. Microb. Biotechnol. 37 (2021) 1–30, https://doi.org/10.1007/s11274-021-03070-x.

[2] Q. Bai, M.M. Liang, W.L. Wu, C.H. Zhang, X. Li, M.H. Liu, D.Q. Yang, W.W. Yu, Q. Hu, L.N. Wang, F.L. Du, N. Sui, Z.L. Zhu, Plasmonic nanozyme of graphdiyne nanowalls wrapped hollow copper sulfide nanocubes for rapid bacteria-killing, Adv. Funct. Mater. 32 (2022), 2112683, https://doi.org/10.1002/adfm.202112683.

[3] Q. Zheng, X. Liu, Y. Zheng, K.W. Yeung, Z. Cui, Y. Liang, Z. Li, S. Zhu, X. Wang, S. Wu, The recent progress on metal–organic frameworks for phototherapy, Chem. Soc. Rev. 50 (2021) 5086–5125, https://doi.org/10.1039/d1cs00056j.

[4] X. Xie, R. Wang, X. Zhang, Y. Ren, T. Du, Y. Ni, H. Yan, L. Zhang, J. Sun, W. Zhang, A photothermal and self-induced Fenton dual-modal antibacterial platform for synergistic enhanced bacterial elimination, Appl. Catal. B Environ. 295 (2021), 120315, https://doi.org/10.1016/j.apcatb.2021.120315.

[5] T.P. Van Boeckel, J. Pires, R. Silvester, C. Zhao, J. Song, N.G. Criscuolo, M. Gilbert, S. Bonhoeffer, R. Laxminarayan, Global trends in antimicrobial resistance in animals in low-and middle-income countries, Science 365 (2019) 1944, https://doi.org/10.1126/science.aaw1944.

[6] R. Yang, G. Song, L. Wang, Z. Yang, J. Zhang, X. Zhang, S. Wang, L. Ding, N. Ren, A. Wang, Full solar-spectrum-driven antibacterial therapy over hierarchical Sn3O4/PDINH with enhanced photocatalytic activity, Small 17 (2021), 2102744, https://doi.org/10.1002/smll.202102744.

[7] B. Ran, Z. Wang, W. Cai, L. Ran, W. Xia, W. Liu, X. Peng, Organic photo-antimicrobials: principles, molecule design, and applications, J. Am. Chem. Soc. 143 (2021) 17891–17909, https://doi.org/10.1021/jacs.1c08679.

[8] G. Liao, F. He, Q. Li, L. Zhong, R. Zhao, H. Che, H. Gao, B. Fang, Emerging graphitic carbon nitride-based materials for biomedical applications, Prog. Mater. Sci. 112 (2020), 100666, https://doi.org/10.1016/j.pmatsci.2020.100666.

[9] J. Li, Z. Li, X. Liu, C. Li, Y. Zheng, K.W.K. Yeung, Z. Cui, Y. Liang, S. Zhu, W. Hu, Interfacial engineering of Bi2S3/Ti3C2Tx MXene based on work function for rapid photo-excited bacteria-killing, Nat. Commun. 12 (2021) 1224, https: //doi.org//s41467-021-21435-6.

[10] P. Li, J. Li, X. Feng, J. Li, Y. Hao, J. Zhang, H. Wang, A. Yin, J. Zhou, X. Ma, Metal-organic frameworks with photocatalytic bactericidal activity for integrated air cleaning, Nat. Commun. 10 (2019) 1–10, https://doi.org/10.1038/s41467-019-10218-9.

[11] W. Wang, H. Xie, G. Li, J. Li, P.K. Wong, T. An, Visible light-induced marine bacterial inactivation in seawater by an in situ photo-fenton system without additional oxidants: implications for ballast water sterilization, ACS EST Water 1 (2021) 1483–1494, https://doi.org/10.1021/acsestwater.1c00048.

[12] X. Yu, S. Wang, X. Zhang, A. Qi, X. Qiao, Z. Liu, M. Wu, L. Li, Z.L. Wang, Heterostructured nanorod array with piezophototronic and plasmonic effect for photodynamic bacteria killing and wound healing, Nano Energy 46 (2018) 29–38, https://doi.org/10.1016/j.nanoen.2018.01.033.

[13] J. Li, Z. Cui, Y. Zheng, X. Liu, Z. Li, H. Jiang, S. Zhu, Y. Zhang, P.K. Chu, S. Wu, Atomic-layer Fe2O3-modified 2D porphyrinic metal-organic framework for enhanced photocatalytic disinfection through electron-withdrawing effect, Appl. Catal. B Environ. 317 (2022), 121701, https://doi.org/10.1016/j.apcatb.2022.121701.

[14] W. Wang, G. Li, T. An, D.K.L. Chan, J.C. Yu, P.K. Wong, Photocatalytic hydrogen evolution and bacterial inactivation utilizing sonochemical-synthesized g-C3N4/red phosphorus hybrid nanosheets as a wide-spectral-responsive photocatalyst: the role of type I band alignment, Appl. Catal. B Environ. 238 (2018) 126–135, https://doi.org/10.1016/j.apcatb.2018.07.004.

[15] Q. Xin, H. Shah, A. Nawaz, W. Xie, M.Z. Akram, A. Batool, L. Tian, S.U. Jan, R. Boddula, B. Guo, Antibacterial carbon-based nanomaterials, Adv. Mater. 31 (2019), 1804838, https://doi.org/10.1002/adma.201804838.

[16] C. Liu, M. Zhang, H. Geng, P. Zhang, Z. Zheng, Y. Zhou, W. He, NIR enhanced peroxidase-like activity of Au@CeO2 hybrid nanozyme by plasmon-induced hot electrons and photothermal effect for bacteria killing, Appl. Catal. B Environ. 295 (2021), 120317, https://doi.org/10.1016/j.apcatb.2021.120317.

[17] X. Yu, X. Jin, X. Chen, A. Wang, J. Zhang, J. Zhang, Z. Zhao, M. Gao, L. Razzari, H. Liu, A microorganism Bred TiO2/Au/TiO2 heterostructure for whispering gallery mode resonance assisted plasmonic photocatalysis, ACS Nano 14 (2020) 13876–13885, https://doi.org/10.1021/acsnano.0c06278.

[18] K. Lee, S. Shin, W.J. Lee, D. Choi, Y. Ahn, M. Park, D. Seo, K. Seo, Sunlight-activatable ROS generator for cell death using TiO2/C-Si microwires, Nano Lett. 21 (2021) 6998–7004, https://doi.org/10.1021/acs.nanolett.1c02337.

[19] C. Liu, D. Kong, P.-C. Hsu, H. Yuan, H.-W. Lee, Y. Liu, H. Wang, S. Wang, K. Yan, D. Lin, Rapid water disinfection using vertically aligned MoS2 nanofilms and visible light, Nat. Nanotechnol. 11 (2016) 1098–1104, https://doi.org/10.1038/nnano.2016.138.

[20] L. Wang, X. Zhang, X. Yu, F. Gao, Z. Shen, X. Zhang, S. Ge, J. Liu, Z. Gu, C. Chen, An all-organic semiconductor C3N4/PDINH heterostructure with advanced antibacterial photocatalytic therapy activity, Adv. Mater. 31 (2019), 1901965, https://doi.org/10.1002/adma.201901965.

[21] H. Cheng, J. Wang, Y. Yang, H. Shi, J. Shi, X. Jiao, P. Han, X. Yao, W. Chen, X. Wei, Ti3C2TX MXene modified with ZnTCPP with bacteria capturing capability and enhanced visible light photocatalytic antibacterial activity, Small (2022), 2200857, https://doi.org/10.1002/smll.202200857.

[22] H. Yin, X. Chen, G. Li, W. Wang, P.K. Wong, T. An, Can photocatalytic technology facilitate conjugative transfer of ARGs in bacteria at the interface of natural sphalerite under different light irradiation? Appl. Catal. B Environ. 287 (2021), 119977 https://doi.org/10.1016/j.apcatb.2021.119977.

[23] L. Wang, B. Li, Z. You, A. Wang, X. Chen, G. Song, L. Yang, D. Chen, X. Yu, J. Liu, Heterojunction of vertically arrayed MoS2 nanosheet/N-doped reduced graphene oxide enabling a nanozyme for sensitive biomolecule monitoring, Anal. Chem. 93 (2021) 11123–11132, https://doi.org/10.1021/acs.analchem.1c01550.

[24] F. Meng, M. Peng, Y. Chen, X. Cai, F. Huang, L. Yang, X. Liu, T. Li, X. Wen, N. Wang, D. Xiao, H. Jiang, L. Xia, H. Liu, D. Ma, Defect-rich graphene stabilized atomically dispersed Cu3 clusters with enhanced oxidase-like activity for antibacterial applications, Appl. Catal. B Environ. 301 (2022), 120826, https://doi.org/10.1016/j.apcatb.2021.120826.

[25] S. Li, B. Xu, M. Lu, M. Sun, H. Yang, S. Liu, Z. Huang, H. Liu, Tensile-strained palladium nanosheets for synthetic catalytic therapy and phototherapy, Adv. Mater. 34 (2022), 2202609, https://doi.org/10.1002/adma.202202609.

[26] Y. Huang, J. Ren, X. Qu, Nanozymes: classification, catalytic mechanisms, activity regulation, and applications, Chem. Rev. 119 (2019) 4357–4412, https://doi.org/10.1021/acs.chemrev.8b00672.

[27] H. Yan, R. Wang, R. Liu, T. Xu, J. Sun, L. Liu, J. Wang, Recyclable and reusable direct Z-scheme heterojunction CeO2/TiO2 nanotube arrays for photocatalytic water disinfection, Appl. Catal. B Environ. 291 (2021) 120096, https://doi.org/10.1016/j.apcatb.2021.120096.

[28] L. Zhang, Z. Liu, Q. Deng, Y. Sang, K. Dong, J. Ren, X. Qu, Nature-inspired construction of MOF@ COF nanozyme with active sites in tailored microenvironment and pseudopodia-like surface for enhanced bacterial inhibition, Angew. Chem. Int. Ed. 60 (2021) 3469–3474, https://doi.org/10.1002/anie.202012487.

[29] Q. Wu, Q, L. Tan, X. Liu, Z. Li, Y. Zhang, Y. Zheng, Y. Liang, Z. Cui, S. Zhu, S. Wu, The enhanced near-infrared photocatalytic and photothermal effects of MXene-based heterojunction for rapid bacteria-killing, Appl. Catal. B Environ. 297 (2021), 120500, https://doi.org/10.1016/j.apcatb.2021.120500.

[30] Y. Chen, P. Wang, H. Hao, J. Hong, H. Li, S. Ji, A. Li, R. Gao, J. Dong, X. Han, Thermal atomization of platinum nanoparticles into single atoms: an effective strategy for engineering high-performance nanozymes, J. Am. Chem. Soc. 143 (2021) 18643–18651, https://doi.org/10.1021/jacs.1c08581.

[31] F. Gao, T. Shao, Y. Yu, Y. Xiong, L. Yang, Surface-bound reactive oxygen species generating nanozymes for selective antibacterial action, Nat. Commun. 12 (2021) 1–18, https://doi.org/10.1038/s41467-021-20965-3.

[32] L. Wang, F. Gao, A. Wang, X. Chen, H. Li, X. Zhang, H. Zheng, R. Ji, B. Li, X. Yu, Defect-rich adhesive molybdenum disulfide/rGO vertical heterostructures with enhanced nanozyme activity for smart bacterial killing application, Adv. Mater. 32 (2020), 2005423, https://doi.org/10.1002/adma.202005423.

[33] G. Fang, R. Kang, Y. Chong, L. Wang, C. Wu, C. Ge, MOF-based DNA hydrolases optimized by atom engineering for the removal of antibiotic-resistant genes from aquatic environment, Appl. Catal. B Environ. 320 (2023), 121931, https://doi.org/10.1016/j.apcatb.2022.121931.

[34] Y. Ai, Z.N. Hu, X. Liang, Hb Sun, H. Xin, Q. Liang, Recent advances in nanozymes: from matters to bioapplications, Adv. Funct. Mater. 32 (2022), 2110432, https://doi.org/10.1002/adfm.202110432.

[35] S. He, J. Huang, Q. Zhang, W. Zhao, Z. Xu, W. Zhang, Bamboo-like nanozyme based on nitrogen-doped carbon nanotubes encapsulating cobalt nanoparticles for wound antibacterial applications, Adv. Funct. Mater. 31 (2021), 2105198, https://doi.org/10.1002/adfm.202105198.

[36] K. Fan, J. Xi, L. Fan, P. Wang, C. Zhu, Y. Tang, X. Xu, M. Liang, B. Jiang, X. Yan, In vivo guiding nitrogen-doped carbon nanozyme for tumor catalytic therapy, Nat. Commun. 9 (2018) 1–11, https://doi.org/10.1038/s41467-018-03903-8.

[37] J. Liu, A. Wang, S. Liu, R. Yang, L. Wang, F. Gao, H. Zhou, X. Yu, J. Liu, C. Chen, A titanium nitride nanozyme for pH-responsive and irradiation-enhanced cascade-catalytic tumor therapy, Angew. Chem. Int. Ed. 60 (2021) 25328–25338, https://doi.org/10.1002/anie.202106750.

[38] Y. Chen, L. Jiao, H. Yan, W. Xu, Y. Wu, H. Wang, W. Gu, C. Zhu, Hierarchically porous S/N codoped carbon nanozymes with enhanced peroxidase-like activity for total antioxidant capacity biosensing, Anal. Chem. 19 (2020) 13518–13524, https://doi.org/10.1021/acs.analchem.0c02982.

[39] J. Zhang, Q. Bai, X. Bi, C. Zhang, M. Shi, W.W. Yu, F. Du, L. Wang, Z. Wang, Z. Zhu, N. Sui, Piezoelectric enhanced peroxidase-like activity of metal-free sulfur doped graphdiyne nanosheets for efficient water pollutant degradation and bacterial disinfection, Nano Today 43 (2022), 101429, https://doi.org/10.1016/j.nantod.2022.101429.

[40] S. Cao, J. Low, J. Yu, M. Jaroniec, Polymeric photocatalysts based on graphitic carbon nitride, Adv. Mater. 27 (2015) 2150–2176, https://doi.org/10.1002/adma.201500033.

[41] W. Wang, T. An, G. Li, D. Xia, H. Zhao, J.C. Yu, P.K. Wong, Earth-abundant Ni2P/g-C3N4 lamellar nanohydrids for enhanced photocatalytic hydrogen evolution and bacterial inactivation under visible light irradiation, Appl. Catal. B Environ. 217 (2017) 570–580, https://doi.org/10.1016/j.apcatb.2017.06.027.

[42] X. Zeng, Y. Liu, Y. Xia, M.H. Uddin, D. Xia, D.T. McCarthy, A. Deletic, J. Yu, X. Zhang, Cooperatively modulating reactive oxygen species generation and bacteria-photocatalyst contact over graphitic carbon nitride by polyethylenimine for rapid water disinfection, Appl. Catal. B Environ. 274 (2020) 119095, https://doi.org/10.1016/j.apcatb.2020.119095.

[43] P. Xia, S. Cao, B. Zhu, M. Liu, M. Shi, J. Yu, Y. Zhang, Designing a 0D/2D S-scheme heterojunction over polymeric carbon nitride for visible-light photocatalytic inactivation of bacteria, Angew. Chem. Int. Ed. 59 (2020) 5218–5225, https://doi.org/10.1002/anie.201916012.

[44] X. Zhang, F. Tian, X. Lan, Y. Liu, W. Yang, J. Zhang, Y. Yu, Building P-doped MoS2/g-C3N4 layered heterojunction with a dual-internal electric field for efficient photocatalytic sterilization, Chem. Eng. J. 429 (2022), 132588, https://doi.org/10.1016/j.cej.2021.132588.

[45] R. Wang, X. Kong, W. Zhang, W. Zhu, L. Huang, J. Wang, X. Zhang, X. Liu, N. Hu, Y. Suo, Mechanism insight into rapid photocatalytic disinfection of Salmonella based on vanadate QDs-interspersed g-C3N4 heterostructures, Appl. Catal. B Environ. 225 (2018) 228–237, https://doi.org/10.1016/j.apcatb.2017.11.060.

[46] B. Wu, Y. Li, K. Su, L. Tan, X. Liu, Z. Cui, X. Yang, Y. Liang, Z. Li, S. Zhu, The enhanced photocatalytic properties of MnO2/g-C3N4 heterostructure for rapid sterilization under visible light, J. Hazard. Mater. 377 (2019) 227–236, https://doi.org/10.1016/j.jhazmat.2019.05.074.

[47] J. Huang, W. Ho, X. Wang, Metal-free disinfection effects induced by graphitic carbon nitride polymers under visible light illumination, Chem. Commun. 50 (2014) 4338–4340, https://doi.org/10.1039/c3cc48374f.

[48] H. Zhao, H. Yu, X. Quan, S. Chen, Y. Zhang, H. Zhao, H. Wang, Fabrication of atomic single layer graphitic-C3N4 and its high performance of photocatalytic disinfection under visible light irradiation, Appl. Catal. B Environ. 152 (2014) 46–50, https://doi.org/10.1016/j.apcatb.2014.01.023.

[49] A. Kumar, P. Raizada, P. Singh, R.V. Saini, A.K. Saini, A.H. Bandegharaei, Perspective and status of polymeric graphitic carbon nitride based Z-scheme photocatalytic systems for sustainable photocatalytic water purification, Chem. Eng. J. 391 (2020), 123496, https://doi.org/10.1016/j.cej.2019.123496.

[50] V. Hasija, A. Kumar, A. Sudhaik, P. Raizada, P. Singh, O.V. Le, T.T. Le, V. H. Nguyen, Step-scheme heterojunction photocatalysts for solar energy, water splitting, CO_2 conversion, and bacterial inactivation: a review, Environ. Chem. Lett. 19 (2021) 2941–2966, https://doi.org/10.1007/s10311-021-01231-w.

[51] L. Wang, X. Tang, Z. Yang, J. Guo, Z. You, Y. Cai, X. Niu, X. Zhang, L. Zhang, J. Zhang, A. Zhu, J. Liu, H. Liu, X. Yu, Regulation of functional groups enable the metal-free PDINH/GO advisable antibacterial photocatalytic therapy, Chem. Eng. J. 451 (2023), 139007, https://doi.org/10.1016/j.cej.2022.139007.

[52] G. Zhang, M. Liu, T. Heil, S. Zafeiratos, A. Savateev, M. Antonietti, X. Wang, Electron deficient monomers that optimize nucleation and enhance the photocatalytic redox activity of carbon nitrides, Angew. Chem. Int. Ed. 131 (2019) 15092–15096, https://doi.org/10.1002/ange.201908322.

[53] H. Lv, Y. Huang, R.T. Koodali, G. Liu, Y. Zeng, Q. Meng, M. Yuan, Synthesis of sulfur-doped 2D graphitic carbon nitride nanosheets for efficient photocatalytic degradation of phenol and hydrogen evolution, ACS Appl. Mater. Interfaces 12 (2020) 12656–12667, https://doi.org/10.1021/acsami.9b19057.

[54] J. Luo, C. Fan, L. Tang, Y. Liu, Z. Gong, T. Wu, X. Zhen, C. Feng, H. Feng, L. Wang, L. Xu, M. Yan, Reveal Brønsted–Evans–Polanyi relation and attack mechanisms of reactive oxygen species for photocatalytic H_2O_2 production, Appl. Catal. B Environ. 301 (2022), 120757, https://doi.org/10.1016/j.apcatb.2021.120757.

[55] Y. Li, S. Wang, W. Chang, L. Zhang, Z. Wu, S. Song, Y. Xing, Preparation and enhanced photocatalytic performance of sulfur doped terminal-methylated g-C3N4 nanosheets with extended visible-light response, J. Mater. Chem. A 7 (2019) 20640–20648, https://doi.org/10.1039/C9TA07014A.

[56] V. Hasija, P. Raizada, A. Sudhaik, K. Sharma, A. Kumar, P. Singh, S. B. Jonnalagadda, V.K. Thakur, Recent advances in noble metal free doped graphitic carbon nitride based nanohybrids for photocatalysis of organic contaminants in water: a review, Appl. Mater. Today 15 (2019) 494–524, https://doi.org/10.1016/j.apmt.2019.04.003.

[57] X. Zhang, P. Zhai, Y. Zhang, Y. Wu, C. Wang, L. Ran, J. Gao, Z. Li, B. Zhang, Z. Fan, Engineering single-atomic Ni-N4-O sites on semiconductor photoanodes for high-performance photoelectrochemical water splitting, J. Am. Chem. Soc. 143 (2021) 20657–20669, https://doi.org/10.1021/jacs.1c07391.

[58] X. Duan, X. Zhou, R. Wang, S. Wang, N.-q Ren, S.-H. Ho, Advanced oxidation processes for water disinfection: features, mechanisms and prospects, Chem. Eng. J. 409 (2021), 128207, https://doi.org/10.1016/j.cej.2020.128207.

[59] D. Chao, Q. Dong, J. Chen, Z. Yu, W. Wu, Y. Fang, L. Liu, S. Dong, Highly efficient disinfection based on multiple enzyme-like activities of Cu_3P nanoparticles: a catalytic approach to impede antibiotic resistance, Appl. Catal. B Environ. 304 (2022), 121017, https://doi.org/10.1016/j.apcatb.2021.121017.

[60] Q. Wu, L. Tan, X. Liu, Z. Li, Y. Zhang, Y. Zheng, Y. Liang, Z. Cui, S. Zhu, S. Wu, The enhanced near-infrared photocatalytic and photothermal effects of MXene-based heterojunction for rapid bacteria-killing, Appl. Catal. B Environ. 297 (2021), 120500, https://doi.org/10.1016/j.apcatb.2021.120500.